JGR Space Physics

RESEARCH ARTICLE
10.1029/2019JA027589

Special Section:
Probing the Magnetosphere through Magnetoseismology and Ultra-Low-Frequency Waves

Simulations of MHD Wave Propagation and Coupling in a 3-D Magnetosphere

Andrew N. Wright[1] **and Thomas Elsden**[2]

[1]Department of Mathematics and Statistics, University of St Andrews, St Andrews, UK, [2]School of Physics and Astronomy, University of Leicester, Leicester, UK

Key Points:
- A simulation grid optimized for MHD wave coupling is described
- Global fast waveguide modes have a mixed standing/propagating nature
- Field line resonances can have a polarization that is far from toroidal

Correspondence to:
A. N. Wright,
anw@st-and.ac.uk

Citation:
Wright, A. N., & Elsden, T. (2020). Simulations of MHD wave propagation and coupling in a 3-D magnetosphere. *Journal of Geophysical Research: Space Physics*, *125*, e2019JA027589. https://doi.org/10.1029/2019JA027589

Received 30 OCT 2019
Accepted 1 FEB 2020
Accepted article online 6 FEB 2020

Abstract A novel simulation grid is devised that is optimized for studying magnetohydrodynamic (MHD) wave coupling and phase mixing in a dipole-like magnetic field. The model also includes flaring on the dawn and dusk flanks. The location of the magnetopause is quite general. In particular, it does not have to coincide with a coordinate surface. Simulations indicate the central role of global fast waveguide modes. These switch from being azimuthally standing in nature at noon, to propagating antisunward on the flanks. The field line resonances (FLRs) seen in the simulation results are three dimensional and not strictly azimuthally polarized. When a plume is present, the FLRs cross a range of 2 in L shell, and have a polarization that is midway between toroidal and poloidal.

1. Introduction

Simulating coupled magnetohydrodynamic (MHD) waves in a realistic magnetic geometry is fraught with difficulties, and every simulation code to date has various advantages and disadvantages. Although the motivation for global nonlinear simulation codes is not strongly biased toward studying the resonant coupling of fast and Alfvén MHD waves (known as field line resonances, FLRs), they are clearly capable of demonstrating this process as shown by Claudepierre et al. (2010) and Ellington et al. (2016).

Global simulations have the advantage of driving the magnetosphere with a self-consistent magnetosheath. The drawback with these codes is normally the use of a Cartesian simulation grid, which is not optimal for studying phase-mixed Alfvén waves: consider an FLR that has a width of 1 R_E in the equatorial plane at $L = 8$, which is resolved by a uniform Cartesian grid of resolution 0.1 R_E. At the ionospheric end the width of the FLR is 0.023 R_E, which is below the uniform grid scale. The issue can be mitigated to some extent by having the inner boundary of the grid at a radius of 4 R_E. However, the FLR width at this boundary is 0.22 R_E, which is still not quite adequately resolved.

Other simulations have opted to sacrifice a self-consistent magnetosheath to focus on resolving the wave coupling process, and do this by using a field-aligned coordinate system. In a 3-D dipole the scalar potential, flux function and azimuth/local time form the basis for an orthogonal set of coordinates, with the potential playing the role of the coordinate along the magnetic field lines. Kageyama et al. (2006) and Proehl et al. (2002) note that while these standard dipole coordinates are appropriate for analytical calculations, they are not suited to numerical work: The main issue is that a grid based upon equal steps in potential would have a disparity in the corresponding real space step size of order 1,000 between grid cells at the equator and the ionosphere, which would render the code too inefficient to be of use.

There is always the option of defining a suitable field-aligned coordinate grid numerically, as has been done in Lee and Lysak (1989) and Proehl et al. (2002). This approach requires the metric scale factors to be determined numerically, which is suitable for computational simulations but not analytical studies. In an effort to retain analyticity Kageyama et al. (2006) show how a particular function of the potential can be used as a suitable field-aligned coordinate. Our approach is similar in spirit to theirs, and we implement it in two stages to provide extra flexibility: First, we determine a coordinate that is equal to path length along **B** on a chosen field line (see Wright & Elsden, 2016 for a 2-D dipole). This essentially flattens the coordinate so equal increments correspond to equal increments in real space. The second step is to define a function of the flattened coordinate to provide enhanced resolution where it is needed. This allows us to tailor our grid in great detail. Our method also has the advantage of providing analytical expressions for the scale factors.

Many of the coordinates described above are based upon a dipole. They have the advantage of being orthogonal, but a drawback in that realistic ionospheric and magnetopause boundaries do not coincide with coordinate surfaces. Proehl et al. (2002), Woodroffe and Lysak (2012), and Lysak et al. (2015) demonstrate how these issues can be addressed, particularly at the ionospheric boundary, by the use of nonorthogonal coordinates. However, the representation of a realistic-shaped magnetopause as a coordinate surface in a simulation employing field-aligned coordinates remains elusive. Simulations in the above studies and those of Degeling et al. (2010), Wright and Elsden (2016), and Elsden and Wright (2018) simply take the magnetopause boundary to coincide with a coordinate surface, which has limited realism, but makes the application of boundary conditions straightforward. In this paper we adopt an equatorial profile for the magnetopause based upon the model given by Shue et al. (1997). Whilst this can capture the flaring nature of the magnetospheric flanks realistically, it comes at the cost of not coinciding with an orthogonal coordinate surface. This makes the application of boundary conditions more difficult, and we show how this can be accommodated using appropriate interpolation.

To date, a single simulation exploiting all the various advantages mentioned above has not been written and may well be some time off. Nevertheless, by considering what each code does best, and treating this as a piece of a jigsaw, a coherent picture of how FLRs are excited and their properties is emerging. Here we introduce and demonstrate the application of two new refinements that may be incorporated in future simulations, namely, optimizing the grid and generalizing the magnetopause boundary location. The paper is structured as follows: Section 2 describes the simulation grid; section 3 describes the simulation details and boundary conditions; section 4 presents simulation results, and section 5 gives some concluding remarks.

2. Model Description

Designing a simulation requires the construction of a suitable coordinate grid. We begin with a description of our orthogonal coordinates, which are formulated by adapting standard 3-D dipole coordinates.

2.1. Standard 3-D Dipole Coordinates $(\chi, \bar{\mu}, \phi)$

In terms of spherical coordinates (r, θ, ϕ) the standard dipole coordinates are (e.g., Kageyama et al., 2006)

$$\chi = \frac{\sin^2\theta}{r}, \qquad \bar{\mu} = -\frac{\cos\theta}{r^2}, \qquad \phi. \tag{1}$$

Here χ and ϕ play the role of Euler potentials and are both constant on a given field line: ϕ labels the azimuth of the meridional plane containing the field line, and χ labels the L shell. In terms of these coordinates an elemental change in position is given by

$$\mathrm{d}\mathbf{r} = \mathbf{e}_\chi h_\chi \mathrm{d}\chi + \mathbf{e}_{\bar{\mu}} h_{\bar{\mu}} \mathrm{d}\bar{\mu} + \mathbf{e}_\phi h_\phi \mathrm{d}\phi, \tag{2}$$

where h_χ, $h_{\bar{\mu}}$, and h_ϕ are scale factors which encompass the geometry of the magnetic field and have the form

$$h_\chi = \frac{r^2}{\sin\theta\sqrt{1+3\cos^2\theta}}, \qquad h_{\bar{\mu}} = \frac{r^3}{\sqrt{1+3\cos^2\theta}}, \qquad h_\phi = r\sin\theta. \tag{3}$$

Figure 1a shows the grid associated with equally spaced increments in χ and $\bar{\mu}$ in a meridian plane. It is evident that the spacing of field lines (shown in black) in the equatorial plane is highly nonuniform. This is to be expected as $\chi = 1/r$ here. It is also apparent that equal steps in $\bar{\mu}$ provide poor resolution near the equator, and excessive resolution at the ionospheric end.

2.2. Modified Dipole Coordinates (α, β, μ)

To address undesirable properties of the $(\chi, \bar{\mu}, \phi)$ coordinates we define modified dipole coordinates (α, β, μ). The first change is a trivial change in notation to replace the azimuthal coordinate ϕ by β. Next we note that if the coordinate χ is constant on a given field line, then any function of χ will also have this property. Exploiting this we define $\alpha = 1/\chi$ as a replacement coordinate. Similarly, we define a new field-aligned coordinate to be $\mu = -r_g^3\bar{\mu}$ (simply a rescaling), where r_g is a reference radius we explain in section 2.2.1.

In terms of (r, θ, ϕ), the modified coordinates (α, β, μ) and their scale factors are

$$\alpha = \frac{r}{\sin^2\theta}, \qquad \beta = \phi, \qquad \mu = \frac{r_g^3\cos\theta}{r^2} \tag{4}$$

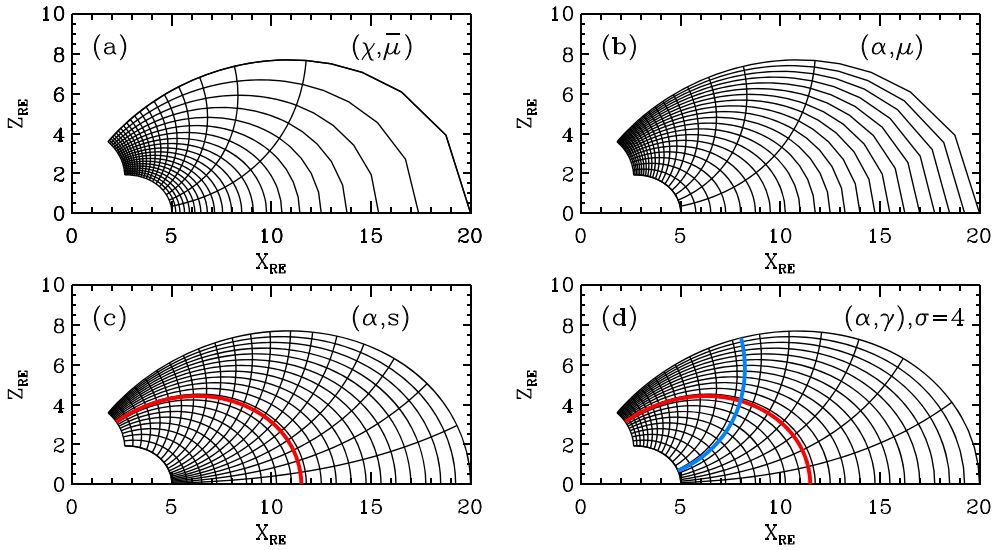

Figure 1. Simulation grids for different coordinates. The grids all cover the same region in real space. To illustrate the properties of different coordinates we take 100 equal steps in each coordinate and plot a contour every fifth step. The panels show (a) dipole coordinates $(\chi, \bar{\mu})$; (b) improved "radial" spacing $(\alpha, \bar{\mu})$; (c) improved field-aligned spacing (α, s); (d) refined resolution at high latitudes (α, γ). The red line represents the $\alpha = r_g$ field line ($r_g = 11.5$). The blue line corresponds to $\gamma = s_l = 6.0$ and denotes the boundary above which the high latitude field-aligned resolution begins to increase.

$$h_\alpha = \frac{\sin^3\theta}{\sqrt{1+3\cos^2\theta}}, \qquad h_\beta = r\sin\theta, \qquad h_\mu = \frac{(r/r_g)^3}{\sqrt{1+3\cos^2\theta}}, \tag{5}$$

where we have used $h_\alpha = h_\chi|\mathrm{d}\chi/\mathrm{d}\alpha|$ and $h_\mu = h_{\bar{\mu}}|\mathrm{d}\bar{\mu}/\mathrm{d}\mu|$. Note in the equatorial plane $\alpha \equiv r$, so has units of length and is similar to the L shell parameter. We have rescaled $\bar{\mu}$ so that μ has units of length. The grid based upon equal increments in α and μ is shown in Figure 1b, and the equal spacing of field lines in the equatorial plane is evident.

To transform the scale factors above to be functions of (α, β, μ) we need to identify relations $r(\alpha, \mu)$ and $\theta(\alpha, \mu)$ to get $h_\alpha(\alpha, \mu)$, $h_\beta(\alpha, \mu)$ and $h_\mu(\alpha, \mu)$. Kageyama et al. (2006) has done this for $(\chi, \bar{\mu})$ (see also Swisdak, 2006), and adapting their results for our (α, μ) gives the following procedure

$$\xi = \left(\frac{\mu\alpha^2}{r_g^3}\right)^2 \tag{6}$$

$$\kappa = \left(9\xi + \sqrt{3}\sqrt{3^3\xi^2 + 4^4\xi^3}\right)^{1/3} \tag{7}$$

$$w = -\frac{c_1}{\kappa} + \frac{\kappa}{c_2\xi}, \qquad (c_1 = 2^{7/3}3^{-1/3}, \quad c_2 = 2^{1/3}3^{2/3}) \tag{8}$$

$$\Upsilon = -\frac{\sqrt{w}}{2} + \sqrt{\frac{1}{2\xi\sqrt{w}} - \frac{w}{4}} \tag{9}$$

which gives the function $\Upsilon(\alpha, \mu)$, from which we can determine r and θ via

$$r = \alpha\Upsilon(\alpha, \mu), \qquad \theta = \arcsin\left(\sqrt{\Upsilon(\alpha, \mu)}\right). \tag{10}$$

Note that arcsin is defined over 0 to π. Substitution of $r(\alpha, \mu)$ and $\theta(\alpha, \mu)$ into (5), renders the formulation solely in terms of (α, β, μ).

2.2.1. Properties of the $\alpha = r_g$ Field Line

We shall identify an analytical relation between the field-aligned coordinate μ and path length on a reference field line for which $\alpha = r_g$—that is, the field line that crosses the equatorial plane at a radial distance of r_g, and is given by (equation (4)) $r = r_g \sin^2\theta$. We begin by identifying the exact path length along this field line, parameterized in terms of θ.

On the $\alpha = r_g$ field line $\mu(r, \theta)$ and $h_\mu(r, \theta)$ vary with θ according to (4) and (5)

$$\mu(r = r_g \sin^2\theta, \theta) = r_g \frac{\cos\theta}{\sin^4\theta}, \qquad h_\mu(r = r_g \sin^2\theta, \theta) = \sin^6\theta / \sqrt{1 + 3\cos^2\theta}. \tag{11}$$

In the equatorial plane $h_\mu(\theta = \pi/2) = 1$, so μ corresponds to path length locally. However, as the poles are approached (θ approaches 0 or π) h_μ becomes very small. As noted by Kageyama et al. (2006), this manifests as a rapidly decreasing grid cell size in real space for equal steps in μ and is evident at the high-latitude section in Figure 1b. This grid also has inadequate field-aligned resolution near the equator.

On $\alpha = r_g$, the exact path length along the field line from the equator is

$$\bar{s}(\theta) = \int_{\pi/2}^{\theta} h_\mu \frac{\mathrm{d}\mu}{\mathrm{d}\theta} \mathrm{d}\theta, \tag{12}$$

and can be integrated (using (11)) to give

$$\frac{\bar{s}(\theta)}{r_g} = \frac{1}{2} \cos\theta \sqrt{1 + 3\cos^2\theta} + \frac{1}{2\sqrt{3}} \sinh^{-1}(\sqrt{3}\cos\theta). \tag{13}$$

The maximum path length is $\bar{s}_{\max} = \bar{s}(\theta = 0)$,

$$\frac{\bar{s}_{\max}}{r_g} = 1 + \frac{1}{2\sqrt{3}} \sinh^{-1}(\sqrt{3}) \equiv 1 + \frac{1}{2\sqrt{3}} \ln(2 + \sqrt{3}) \approx 1.380173 \tag{14}$$

2.3. The (α, β, s) Coordinates

In a 2-D dipole geometry Wright and Elsden (2016) exploited the fact that, on a chosen field line, the exact path length could be expressed as a function of the scalar potential. They then used this path length as a new field-aligned coordinate, which afforded a more computationally efficient grid. This approach is not so straightforward with a 3-D dipole as the functional relation between potential and path length is not invertible. (It is not possible to use (13) to provide an explicit expression for $\theta(\bar{s})$.) However, it is possible to determine an approximation to this function explicitly, and this is a key step in our grid formulation. The relation we derive below is a basic property of a 3-D dipole field, and may have relevance in a broad range of studies which employ a 3-D dipole.

We begin by introducing a new coordinate, $s(\mu)$. Here s corresponds closely to path length on the $\alpha = r_g$ field line, that is, it is an approximation to the exact path length $\bar{s}$ given in (13). The behavior of $\mu(s)$ is radically different at the equator and the poles, so we consider series expansions at $\theta = 0$, $\pi/2$ and π of $\bar{s}(\theta)$ and $\mu(\theta)$ using equations (11) and (13).

$$\frac{s(\theta)}{r_g} \approx \begin{cases} \dfrac{\bar{s}_{\max}}{r_g} - \theta^2 + \mathcal{O}(\theta^4), & \theta \to 0 \\ \dfrac{\pi}{2} - \theta + \mathcal{O}((\theta - \pi/2)^3), & \theta \approx \pi/2 \\ -\dfrac{\bar{s}_{\max}}{r_g} + (\pi - \theta)^2 + \mathcal{O}((\pi - \theta)^4), & \theta \to \pi \end{cases} \tag{15}$$

$$\frac{\mu(\theta)}{r_g} \approx \begin{cases} \dfrac{1}{\theta^4} + \mathcal{O}(\theta^{-2}), & \theta \to 0 \\ \dfrac{\pi}{2} - \theta + \mathcal{O}((\theta - \pi/2)^3), & \theta \approx \pi/2 \\ -\dfrac{1}{(\pi - \theta)^4} + \mathcal{O}((\pi - \theta)^{-2}), & \theta \to \pi. \end{cases} \tag{16}$$

Eliminating θ between (15) and (16) allows series expansions for $\mu(s)$ to be found at $s = -\bar{s}_{max}$, 0 and $\bar{s}_{max}$

$$\frac{\mu(s)}{r_g} \approx \begin{cases} \left(\frac{\bar{s}_{max}}{r_g} - \frac{s}{r_g}\right)^{-2}, & s \to \bar{s}_{max} \\ \frac{s}{r_g}, & |s/r_g| \ll 1 \\ -\left(\frac{\bar{s}_{max}}{r_g} + \frac{s}{r_g}\right)^{-2}, & s \to -\bar{s}_{max}. \end{cases} \tag{17}$$

After some experimentation the following empirical form for $\mu(s)$ was settled on.

$$\frac{\mu(s)}{r_g} = \frac{s/r_g + a_1(s/r_g)^3}{1 + (a_2 s/r_g)^4} \pm \frac{1}{(\bar{s}_{max}/r_g \mp s/r_g)^2} \times \frac{(s/r_g)^4}{a_3 + (s/r_g)^4} \tag{18}$$

The upper signs are for $s > 0$, the lower for $s < 0$, and a_1, a_2 and a_3 are parameters used to tune the fit. The form of (18) was motivated by the fact that as $s/r_g \to 0$ the first term dominates and matches the expansion in (17). Similarly, as $s \to \pm\bar{s}_{max}$ and $a_3 \to 0$ the second term dominates and produces the series solutions in (17).

The parameters $a_1 = 0.7$, $a_2 = 0.5$, and $a_3 = 2/3$ were chosen to optimize the overall fit of the empirical formula so that $s \approx \bar{s}$ to a high degree. This was achieved as follows: choose a value for s; use (18) to determine μ; find θ on the $\alpha = r_g$ field using $\theta(\alpha = r_g, \mu)$ in (10); finally, the exact path length can then be found as $\bar{s}(\theta)$ in (13) and compared with the initial value of s. Using the values of the coefficients quoted above the discrepancy between s and $\bar{s}$ was 1% or less over $-1.38 < s/r_g < 1.38$ (i.e., the entire length of the field line). This is more than adequate for our purposes.

Figure 1c shows the grid for equally spaced increments of α and s. Notice that on the $\alpha = r_g$ field line (shown in red) the grid has equal steps in path length when advancing along the field line. The importance of the parameter r_g can be appreciated by studying Figure 1c. It is evident that for field lines beyond the red field line ($\alpha > r_g$) the separation of the contours of s is always greater than that on the red field line. A close inspection of these field lines (e.g., the one passing through $(X, Z) = (20,0)$) shows that the step size along the field line is large at the equator and decreases on moving to higher latitudes. The opposite is true for field lines with ($\alpha < r_g$): Now the separation of the contours of s is always less than that on the red field line. Moreover, on these field lines (e.g., the one passing through $(X, Z) = (5,0)$) the step size along the field line is small at the equator and increases on moving to higher latitudes.

The distortion of the s coordinate from representing real path length when away from the $\alpha = r_g$ field line is unavoidable when using dipole-based coordinates. However, by placing the r_g field line somewhere in the middle of our domain, excessive distortions of grid spacing can be avoided when compared to having the $\alpha = r_g$ field line on either the inner or outer boundary. This allows for more efficient computation.

For coordinates (α, β, s) the scale factor $h_s(\alpha, s)$ can be found from

$$h_s(\alpha, s) = h_\mu(\alpha, \mu(s)) \times \left|\frac{d\mu}{ds}\right| \tag{19}$$

and $d\mu/ds$ is found by differentiating equation (18). This shows the advantage of having an analytical definition of the relation between μ and s, namely, that we can determine h_s exactly by evaluating an analytical function. If the analytical relation did not exist, we would have to estimate h_s numerically by a separate computation.

2.4. Simulation Coordinates (α, β, γ)

The main advantage of field-aligned coordinates when studying phase-mixed Alfvén waves is that the small scales which develop perpendicular to **B** can be resolved using several hundreds of grid points in these directions—in contrast to the field-aligned direction, which will not contain small scales and will need <100 grid points. The main factor relevant to optimizing the field-aligned coordinate is the fact that the there is a scale length associated with the variation of the background field strength and scale factors, which decreases with increasing latitude. This means that our optimal field-aligned coordinate will have a finer spatial resolution at high latitudes compared to low latitudes.

Now that we have a field-aligned coordinate (s) that is effectively uniform along our reference field line, it is a simple matter to define a new field-aligned coordinate $\gamma(s)$ which we can tailor to provide a finer grid where necessary. Depending upon the focus of the simulation, there are many options for the form of $\gamma(s)$, and we choose a simple illustrative one here.

For the final coordinate change $(\alpha, \beta, s) \rightarrow (\alpha, \beta, \gamma(s))$ we set

$$\frac{\gamma(s)}{r_g} = \begin{cases} \frac{s}{r_g} + \frac{\upsilon}{3}\left(\frac{s}{r_g} - \frac{s_l}{r_g}\right)^3, & s_l < s < s_u \\ \frac{s}{r_g}, & -s_l \le s \le s_l \\ \frac{s}{r_g} + \frac{\upsilon}{3}\left(\frac{s}{r_g} + \frac{s_l}{r_g}\right)^3, & -s_u < s < -s_l. \end{cases} \tag{20}$$

The upper limit of the s domain is s_u, and we assume grid symmetry about the equator ($s = 0$). A lower value of s, namely s_l, is used to define a region around the equator ($-s_l \le s \le s_l$) where a finer grid is not needed, so we let $\gamma = s$ here. The functional form (20) was chosen as $\gamma(s)$ and its first two derivatives are continuous at $s = \pm s_l$.

The difference in grid spacing between the s grid and the γ grid (Δs and $\Delta\gamma$) when at high latitudes can be appreciated by noting $\Delta\gamma/\Delta s \approx \mathrm{d}\gamma/\mathrm{d}s$. Differentiating (20) to give

$$\frac{\mathrm{d}\gamma(s)}{\mathrm{d}s} = \begin{cases} 1 + \upsilon\left(\frac{s}{r_g} - \frac{s_l}{r_g}\right)^2, & s_l < s < s_u \\ 1, & -s_l \le s \le s_l \\ 1 + \upsilon\left(\frac{s}{r_g} + \frac{s_l}{r_g}\right)^2, & -s_u < s < -s_l \end{cases} \tag{21}$$

shows the relative density of grid points in γ to s (i.e., $\mathrm{d}\gamma/\mathrm{d}s$) is evidently controlled by υ. At the end of the field line ($s = s_u$) the relative density of grid points in γ compared to s has increased by a factor $\sigma = \mathrm{d}\gamma/\mathrm{d}s|_{s_u}$.

$$\sigma = 1 + \upsilon\left(\frac{s_u}{r_g} - \frac{s_l}{r_g}\right)^2. \tag{22}$$

Inverting for υ gives

$$\upsilon = \frac{\sigma - 1}{\left(\frac{s_u}{r_g} - \frac{s_l}{r_g}\right)^2}. \tag{23}$$

If, for example, we required the density of grid points to increase by a factor of 4 at $s = s_u$ compared to that at $s = s_l$, we set $\sigma = 4$ in (23) to determine the required υ, which then defines the γ coordinate through (20). Figure 1d illustrates this for $\sigma = 4$. The increase in field-aligned resolution is particularly evident when comparing the grids at the high-latitude ends of the field lines passing through $(X, Z) = (5, 0)$ in Figures 1c and 1d. The line $s = s_l$ is also highlighted and represents where the field-aligned grid refinement commences.

It will also be necessary to invert $\gamma(s)$ to give $s(\gamma)$. Inverting (20) gives

$$\frac{s(\gamma)}{r_g} = \begin{cases} \frac{M(\gamma, s_l, r_g, \upsilon)}{(2\upsilon)^{1/3}} - \frac{2^{1/3}}{\upsilon^{2/3} M(\gamma, s_l, r_g, \upsilon)} + s_l, & s_l < \gamma < \gamma(s_u) \\ \frac{\gamma}{r_g}, & -s_l \le \gamma \le s_l \\ \frac{M(\gamma, -s_l, r_g, \upsilon)}{(2\upsilon)^{1/3}} - \frac{2^{1/3}}{\upsilon^{2/3} M(\gamma, -s_l, r_g, \upsilon)} - s_l, & \gamma(-s_u) < s < -s_l, \end{cases} \tag{24}$$

where

$$M(\gamma, s', r_g, \upsilon) = \left(3\left(\frac{\gamma}{r_g} - \frac{s'}{r_g}\right) + \sqrt{9\left(\frac{\gamma}{r_g} - \frac{s'}{r_g}\right)^2 + \frac{4}{\upsilon}}\right)^{1/3} \tag{25}$$

and the dummy argument s' can have the values $-s_l$ or $+s_l$.

2.5. Summary of Coordinates and Scale Factors

1. Choose the boundaries of the domain: begin with the upper and lower α limits. Azimuth runs over $-\pi < \beta < \pi$. We also choose grid parameters r_g and s_u. Next we choose the grid refinement lower bound (s_l) and grid point density enhancement factor (σ), and determine υ with equation (23). The limits of the γ grid are $\gamma(\pm s_u)$ from equation (20). We can now set up uniform grids in α, β and γ space.
2. Calculate $h_\alpha(\alpha,\beta,\gamma)$ and $h_\beta(\alpha,\beta,\gamma)$ on the grid as follows: use (24) to convert γ to corresponding s, and use (18) to find the corresponding μ value. Next use equation (10) to transform (α,μ) to (r,θ) and finally use (5) to find h_α and h_β at the required point.
3. Calculation of $h_\gamma(\alpha,\beta,\gamma)$: Follow the same steps as above for h_α and h_β, using (5) to find h_μ at the grid point. h_γ may be found by noting

$$h_\gamma = h_s\left|\frac{\mathrm{d}s}{\mathrm{d}\gamma}\right| = h_\mu\left|\frac{\mathrm{d}\mu}{\mathrm{d}s}\right|\left|\frac{\mathrm{d}s}{\mathrm{d}\gamma}\right| = h_\mu\left|\frac{\mathrm{d}\mu}{\mathrm{d}s}\right|\left|\frac{\mathrm{d}\gamma}{\mathrm{d}s}\right|^{-1}, \tag{26}$$

and $\mathrm{d}\mu/\mathrm{d}s$ is found from differentiating (18). The penultimate expression in (26) could be evaluated by finding $\mathrm{d}s/\mathrm{d}\gamma$ from differentiating (24), but it is easier to evaluate the final expression in (26) and use $\mathrm{d}\gamma/\mathrm{d}s$ as given in (21).

3. Simulation Details

3.1. Governing Equations

Simulation variables U_α, U_β, B_α, B_β, and B_γ are related to plasma velocity $\mathbf{u}$ and magnetic field perturbation $\mathbf{b}$ by $U_\alpha = u_\alpha h_\beta B$ (B is the background magnetic field strength), $U_\beta = u_\beta h_\alpha B$, $B_\alpha = b_\alpha h_\alpha$, $B_\beta = b_\beta h_\beta$, and $B_\gamma = b_\gamma h_\gamma$. The equations are normalized as follows: lengths by $L_0 = 6,371$ km, an Earth radius; speeds by the Alfvén speed $V_0 = 757.427$ km s^{-1} at the inner boundary $(X,Y,Z) = (5,0,0)$; magnetic fields by the background field at $(5,0,0)$, $B_0 = 300$ nT; time is normalized by $T_0 = L_0/V_0 = 8.411$ s

$$\frac{\partial U_\alpha}{\partial t} = V^2\frac{h_\beta}{h_\alpha h_\gamma}\left[\frac{\partial B_\alpha}{\partial\gamma} - \frac{\partial B_\gamma}{\partial\alpha}\right] - \nu U_\alpha \tag{27}$$

$$\frac{\partial U_\beta}{\partial t} = V^2\frac{h_\alpha}{h_\beta h_\gamma}\left[\frac{\partial B_\beta}{\partial\gamma} - \frac{\partial B_\gamma}{\partial\beta}\right] - \nu U_\beta \tag{28}$$

$$\begin{aligned}\frac{\partial B_\alpha}{\partial t} =& \frac{h_\alpha}{h_\beta h_\gamma}\frac{\partial U_\alpha}{\partial\gamma} - \frac{h_\alpha}{h_\beta h_\gamma}\left[\frac{\partial}{\partial\beta}\left\{\frac{\eta h_\gamma}{h_\alpha h_\beta}\left(\frac{\partial B_\beta}{\partial\alpha} - \frac{\partial B_\alpha}{\partial\beta}\right)\right\}\right.\\ &\left. - \frac{\partial}{\partial\gamma}\left\{\frac{\eta h_\beta}{h_\alpha h_\gamma}\left(\frac{\partial B_\alpha}{\partial\gamma} - \frac{\partial B_\gamma}{\partial\alpha}\right)\right\}\right]\end{aligned} \tag{29}$$

$$\begin{aligned}\frac{\partial B_\beta}{\partial t} =& \frac{h_\beta}{h_\alpha h_\gamma}\frac{\partial U_\beta}{\partial\gamma} - \frac{h_\beta}{h_\alpha h_\gamma}\left[\frac{\partial}{\partial\gamma}\left\{\frac{\eta h_\alpha}{h_\beta h_\gamma}\left(\frac{\partial B_\gamma}{\partial\beta} - \frac{\partial B_\beta}{\partial\gamma}\right)\right\}\right.\\ &\left. - \frac{\partial}{\partial\alpha}\left\{\frac{\eta h_\gamma}{h_\alpha h_\beta}\left(\frac{\partial B_\beta}{\partial\alpha} - \frac{\partial B_\alpha}{\partial\beta}\right)\right\}\right]\end{aligned} \tag{30}$$

$$\begin{aligned}\frac{\partial B_\gamma}{\partial t} =& -\frac{h_\gamma}{h_\alpha h_\beta}\left[\frac{\partial U_\alpha}{\partial\alpha} + \frac{\partial U_\beta}{\partial\beta}\right] - \frac{h_\gamma}{h_\alpha h_\beta}\left[\frac{\partial}{\partial\alpha}\left\{\frac{\eta h_\beta}{h_\alpha h_\gamma}\left(\frac{\partial B_\alpha}{\partial\gamma} - \frac{\partial B_\gamma}{\partial\alpha}\right)\right\}\right.\\ &\left. - \frac{\partial}{\partial\beta}\left\{\frac{\eta h_\alpha}{h_\beta h_\gamma}\left(\frac{\partial B_\gamma}{\partial\beta} - \frac{\partial B_\beta}{\partial\gamma}\right)\right\}\right].\end{aligned} \tag{31}$$

Here V is the Alfvén speed, ν is a linear drag term and η the resistivity. The above equations are the components of the momentum and induction equations written in our curvilinear coordinates (α,β,γ) and simulation variables. They are the same as in Elsden and Wright (2017), except that we now include a nonzero η in Ohm's Law.

3.2. Grid and Boundary Conditions

We employ a staggered grid with constant spacing $\Delta\alpha$, $\Delta\beta$, and $\Delta\gamma$. If a unit cell of the lattice with sides $\Delta\alpha$, $\Delta\beta$, and $\Delta\gamma$ has B_γ defined at (0,0,0) and its corners, then U_α is defined at $(\Delta\alpha/2,0,0)$, U_β at $(0,\Delta\beta/2,0)$, B_α at $(\Delta\alpha/2,0,\Delta\gamma/2)$, and B_β at $(0,\Delta\beta/2,\Delta\gamma/2)$. The equations are solved over the domain $\alpha_{\min} < \alpha < \alpha_{\max}(\beta)$, $-\pi < \beta < \pi$, and $0 < \gamma < \gamma(s_u)$. $\alpha_{\max}(\beta)$ is taken to be the radial distance to the equatorial magnetopause in the model described by Shue et al. (1997), and produces the flaring on the flanks evident in Figure 3.

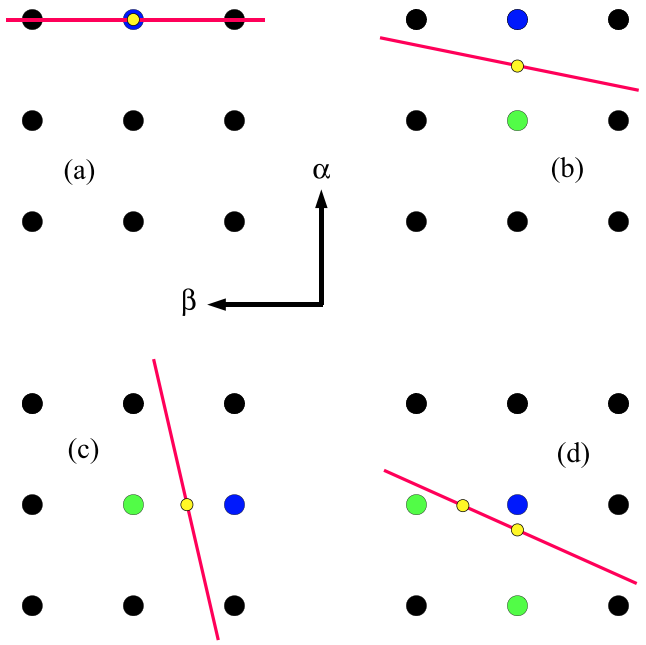

Figure 2. The outer edge of the (α, β) grid (at constant γ) on which B_γ values are calculated. The red line represents the magnetopause. The blue dot is a grid point where we specify B_γ to drive the simulation. The yellow dot is a point on the magnetopause where a prescribed driver defines the value of B_γ. Four configurations are considered. In (a) the magnetopause coincides with the grid. In (b)–(d) the magnetopause does not coincide with the grid, and interior points (green) are used with interpolation to define the value at the blue point.

3.2.1. Ionospheric Boundary

The ionospheric boundary is located at $\gamma = \gamma(s_u)$, where nodes of velocity and B_γ are enforced. Antinodes of B_α and B_β are also applied here. These boundary conditions are perfectly reflecting.

3.2.2. Inner Boundary

The inner boundary of the domain was taken to be the plasmapause, beyond which would be the dense plasmasphere. For simplicity, we assumed the large jump in density on crossing the plasmapause would produce wave reflection which we model by imposing nodes of U_α and B_α (and antinodes of U_β, B_β, and B_γ) on the L shell $\alpha = \alpha_{\min}$.

3.2.3. Magnetopause Boundary

The magnetopause boundary coincides with the surface $\alpha_{\max}(\beta)$, which is taken to be the radial distance to the equatorial magnetopause in the model described by Shue et al. (1997). In our notation this gives

$$\alpha_{\max}(\beta) = r_0 \left(\frac{2}{1 + \cos(\beta)} \right)^{\hat{\alpha}} \tag{32}$$

where r_0 is the distance to the subsolar magnetopause, and the index $\hat{\alpha}$ (simply α in Shue et al., 1997) controls the degree of flaring on the flanks evident in Figure 3. In the axisymmetric magnetic field employed in Elsden and Wright (2017, 2018), the edge of the staggered grid coincided with a surface $\alpha_{\max} = \text{const.}$, and the only quantity needing to be defined there was B_γ (a proxy for the magnetic pressure). This corresponds to the situation in Figure 2a, where the red line shows the magnetopause in a surface of constant γ along with the grid points in α and β. The yellow dot represents a point on the magnetopause where driving condition gives the value of B_γ, and the blue dot is a boundary grid point where we need to specify B_γ. As the yellow and blue dots coincide we can simply assign the driven value (yellow) to the blue dot at both the predictor and corrector steps of the Leap-frog Trapezoidal algorithm for all boundary points to drive the simulation (Elsden & Wright, 2017).

In Figures 2b–2d the situation is not so simple as the magnetopause moves "radially" in α with azimuth β. The driving condition still defines B_γ everywhere on the magnetopause (red line), but this does not coincide with grid points. On moving to larger α, the first grid cell after crossing the magnetopause is designated as a ghost cell (colored blue in panels b–d). If we are able to define a suitable value for B_γ on the ghost cells, then the integration algorithm can update all the interior points. For the situation in Figure 2b, this is relatively straightforward: We have a preexisting value at the first interior grid point (green), and the prescribed driver defines the value on the magnetopause at the yellow dot. We can then use linear interpolation to infer a value for the ghost cell (blue). If this is repeated for all ghost cells, then the entire interior grid can be updated.

If the orientation of the magnetopause is like that shown in Figure 2c, a similar procedure can be used to that above, except that the first interior grid point (green) is found by moving in β. Now interpolation in β using the value on the magnetopause (yellow) and preexisting interior value (green) is used to calculate the ghost cell (blue) value. There is one problem with this approach: If the yellow and green dots are very close together (less than 10^{-2} of the grid cell size), then interpolation to the blue dot will have large errors and renders the method too inaccurate to be of use. After some experimentation a simple work-around was found: When the green and yellow dots are too close, we simply assume they coincide and assign the value of the yellow dot to the green dot (which is then treated as a boundary point, rather than in interior point), which becomes similar to the situation in Figure 2a.

The final case we need to consider is shown in Figure 2d. Here, the ghost cell value could be determined by interpolating in either α or β using the pairs of green and yellow dots shown. Performing both these interpolations gives two possible values to be assigned to the ghost cell (blue), and these values will not be identical. In this situation we take an average of the two possible values, and weight the average based upon the (real space) distance from the blue to the yellow dots. For the situation in Figure 2d, the nearest yellow

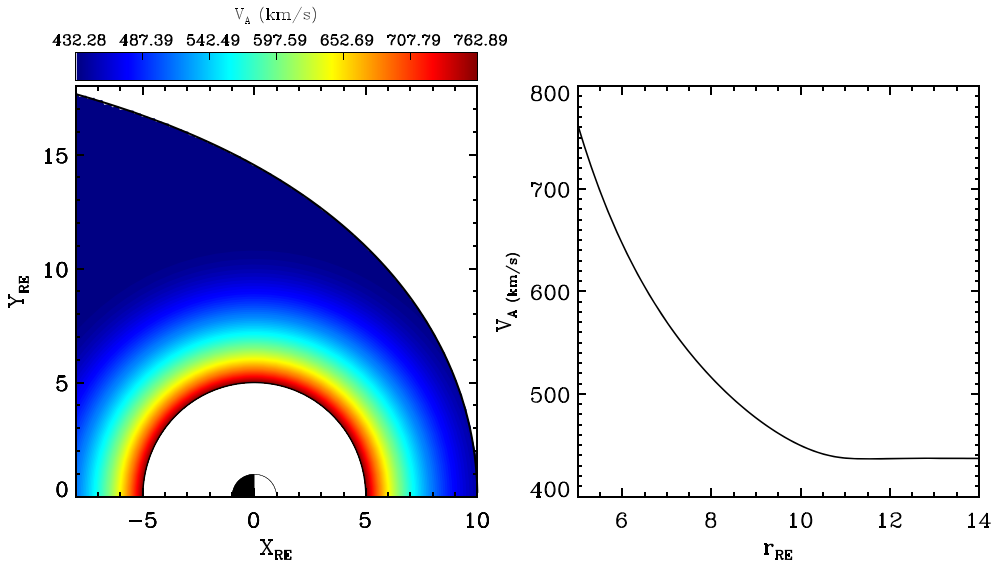

Figure 3. Variation of V_A in the equatorial plane used in Figures 4–10.

dot to the ghost cell lies in the alpha direction. Since we know B_γ at the yellow dots, it is sensible to give the ghost cell value based upon the α interpolation of the higher weighting.

3.3. Nightside Boundary

The simulation is designed to study the propagation and coupling of MHD waves on the dayside and flanks. In practice, antisunward propagating waves may travel into the tail, where they will be lost from the domain of interest to us. Specifically, we simulate waves in the region $x > -6\,R_E$. We do not model the magnetotail in detail, but simply treat it as a region we can lose wave energy to irreversibly. We mimic this property by adding a buffer zone for $-9\,R_E < x < -6\,R_E$ where the drag coefficient ν is nonzero. Tests showed that this works well as negligible wave energy reached the end of our domain (at $x = -9\,R_E$) nor was there evidence of reflected waves propagating sunward from the buffer zone.

3.4. Numerical Details

The code is parallelized by introducing subgrids in the α and β directions to allow fine spatial resolution in these directions to resolve phase-mixed Alfvén waves. The subgrids were only extended in α ("radially") as far as is necessary to cover the magnetopause, hence local times where there is more flaring of the magnetopause need more subgrids. The numerical integration algorithm we employ is the Leap-frog Trapezoidal scheme of Zalesak (1979), and the equations are driven by specifying the magnetic pressure on the magnetopause at the predictor and corrector steps, as described in Elsden and Wright (2017).

Some form of dissipation is necessary to prevent Alfvén waves phase mixing below the grid scale (Mann et al., 1995). The main dissipation of Alfvén wave energy is in the ionosphere through Joule heating of Pedersen currents. Interestingly, the ionosphere is a much better reflector of the fast mode than the Alfvén mode (Kivelson & Southwood, 1988). The use of resistivity allows us to mimic this bias: it will cause significant dissipation of Alfvén waves since they have a relatively small transverse scale and large current density compared to the fast mode. In contrast the drag term ($-\nu\mathbf{u}$) acts equally on both waves and would cause unwanted decay of the fast mode. (We reserve the use of drag for the buffer zone where we intentionally want to dissipate both wave modes.) The use of resistivity in the domain of interest described in the previous subsection also has the advantage that most of the dissipation will occur at higher latitudes (where the field-aligned current is stronger). Consequently, virtual satellites at lower latitudes will observe a Poynting vector showing a poleward flow of energy similar to that found with ionospheric dissipation. However, virtual low-altitude satellites will not have a realistic Poynting vector signature. The value of η is chosen to give FLR widths of $\sim$1 R_E in the equatorial plane.

The size of the time step in our simulation is constrained by requiring it to resolve the propagation time across a grid cell ($\sim \delta/V$, the CFL condition) and also the diffusion time across a grid cell ($\sim \delta^2/\eta$), where

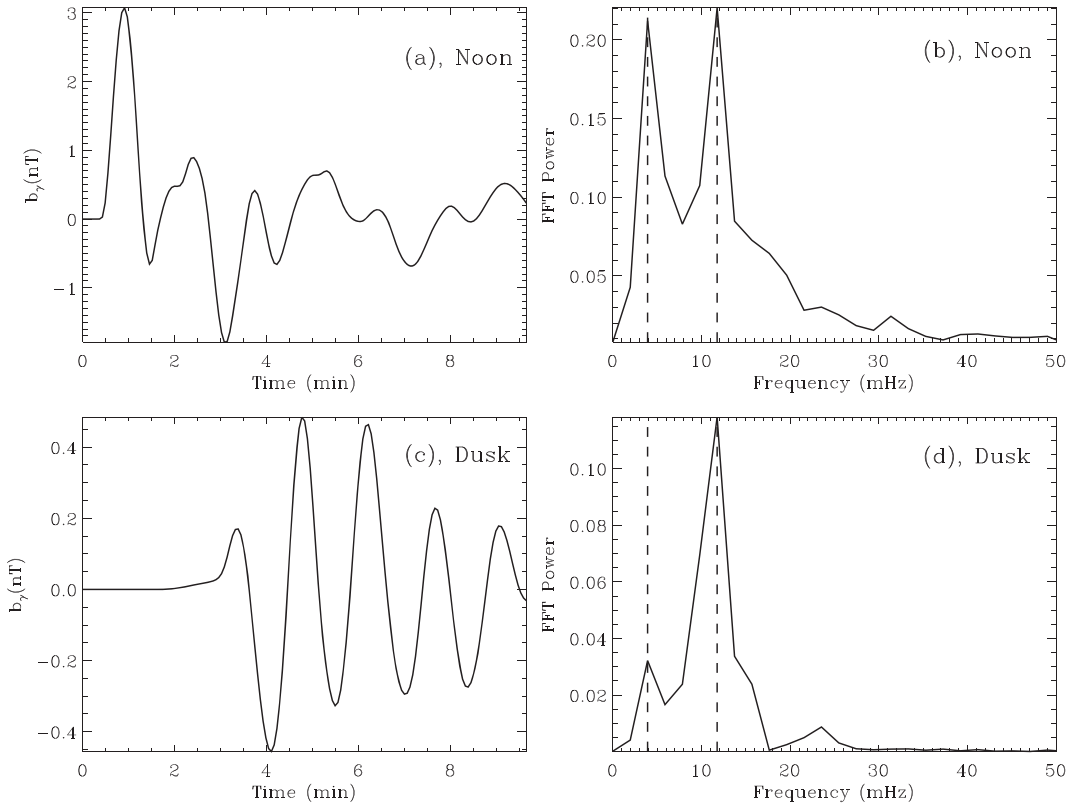

Figure 4. Variation of the compressional magnetic field in time at (a) noon and (c) dusk. FFTs show the same two frequencies (at 3.9 and 11.8 mHz) present at noon (b) and dusk (d).

δ is approximately the smallest real space extent of a grid cell. The δ^2 scaling of the diffusion time means it becomes impractical to resolve at high latitudes. We avoid this difficulty by having a uniform η throughout the vast majority of our domain, but smoothly reduce it to zero as the ionospheric boundary is approached. (Specifically, we let η have the following dependence on γ: over $|\gamma| < 0.6\gamma_{\max}$ the value of η is held constant at the value we quote below, whereas over $|\gamma| > 0.8\gamma_{\max}$ the resistivity is set to zero. Between these two regions the resistivity varies in a continuous and differentiable fashion.) Thus, our time step is constrained by the CFL condition $\Delta t < \delta/V$ and is generally associated with the width of the grid in α at the high-latitude boundary.

Test runs used to benchmark the accuracy of the code when the dissipative terms are present shows that energy continuity is balanced to 1 part in 10^4. The simulation results in the remainder of the paper use a grid of $200 \times 200 \times 50$ points, $s_l = 8.0$, $s_u = 12.0$, $\sigma = 3.0$, $\gamma_{\max} = 14.667$, $\eta = 0.004$, $\nu = 8.0$, $\Delta t = 2 \times 10^{-4}$, and employ the axisymmetric equatorial Alfvén speed variation shown in Figure 3 (unless stated otherwise). There is an additional variation of Alfvén speed along the field lines through the density dependence $n = n_{\text{eq}}(\alpha)(r_{\text{eq}}/r)^4$ (based upon the theoretical estimate shown in Figure 1 of Angerami & Carpenter, 1966). The Alfvén speed profile is intended to represent a typical magnetosphere that is broadly consistent with observations and theory: Figure 1 of Archer et al. (2015), Figures 2a and 2b of Moore et al. (1987), Takahashi and Anderson (1992).

3.5. Magnetopause Driving

The magnetopause is driven by applying a magnetic pressure perturbation on the magnetopause that represents a jolt given to the system from an interplanetary shock. We employ drivers that are either symmetric or antisymmetric about noon, but assume symmetry about the equatorial plane in this paper. The explicit form of the symmetric driver is

$$b_\gamma(\beta, \gamma, t) = \cos^2(k_\beta \beta)\cos^2(k_\gamma \gamma)\sin^2(\pi t/\tau_d), \tag{33}$$

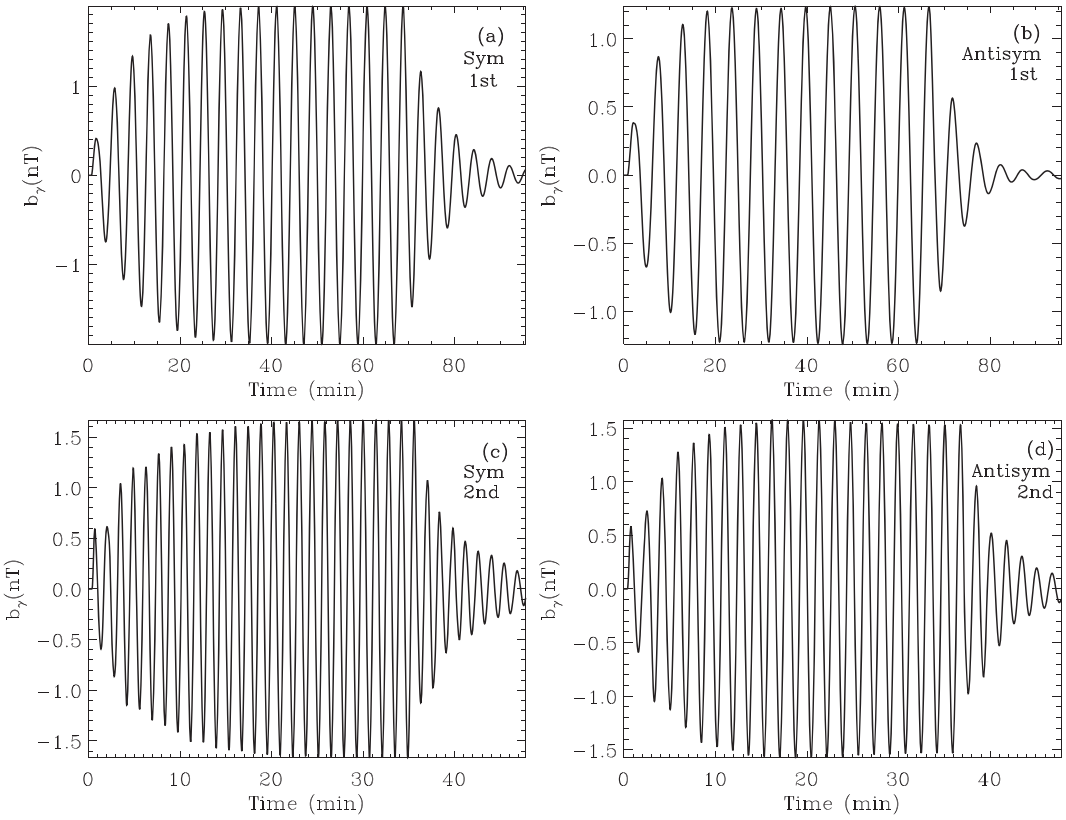

Figure 5. Time variation of the $b_\gamma(t)$ when driven to excite the first and second radial harmonic symmetric wave guide modes ((a) $(X, Y) = (6.79, 0)$ and (c) $(X, Y) = (8.22, 0)$), and the first and second radial harmonic antisymmetric waveguide modes ((b) $(X, Y) = (5.06, 4.53)$ and (d) $(X, Y) = (7.77, 3.64)$).

imposed over $-1 \le \beta \le 1$, $0 \le \gamma \le 6$ and up until time $t = \tau_d = 10.0$, after which the driver is set to 0. The wave numbers are given by $k_\beta = \pi/2$ and $k_\gamma = 2\pi/\lambda_\gamma = \pi/12$. (All these quantities are given in normalized simulation units—see section 3.1.) In dimensional units, the full width at half maximum (FWHM) in the equatorial plane of the β profile is about 10 R_E, and the field-aligned FWHM is 6 R_E in the noon meridian. The subsolar magnetopause is at $(X, Y, Z) = (10, 0, 0)$ and there is no dipole tilt. The flaring of the magnetopause is governed by the choice $r_0 = 10\ R_E$ and $\hat{\alpha} = 0.54$ in equation (32).

4. Simulation Results

The natural fast waveguide frequencies of the equilibrium can be explored by looking at $b_\gamma(t)$ at different locations in the magnetosphere as this field will be a signature of the fast mode. Figure 4 shows $b_\gamma(t)$ in the equatorial plane at noon ($(X, Y) = (8.14, 0.0)$) and at dusk ($(X, Y) = (-1.55, 12.44)$). The longer propagation time to dusk is evident by the time delay in Figure 4c.

4.1. Waveguide Modes

Figures 4b and 4d show the FFTs of the signals from noon and dusk. It is noteworthy that the FFTs show the same two natural frequencies present. Elsden and Wright (2018) interpret this property as follows: Following the driving phase the subsequent behavior of the magnetosphere can be described as a sum over the normal modes of the system, with each oscillating freely at their natural frequencies. Since the modes are global, it follows that a spacecraft at both noon and dusk will see the same frequencies following the driving phase – as is clearly exhibited in Figure 4. It may be thought that these frequencies should be related, in some way, to the driving time scale τ_d. Wright and Rickard (1995) show that the values of these frequencies are actually a property of the medium, not of the driver. However, the amplitude of the FFT peaks does depend upon the driver: it is necessary for the FFT of the driver to have significant power at the waveguide mode frequencies if they are to be excited significantly.

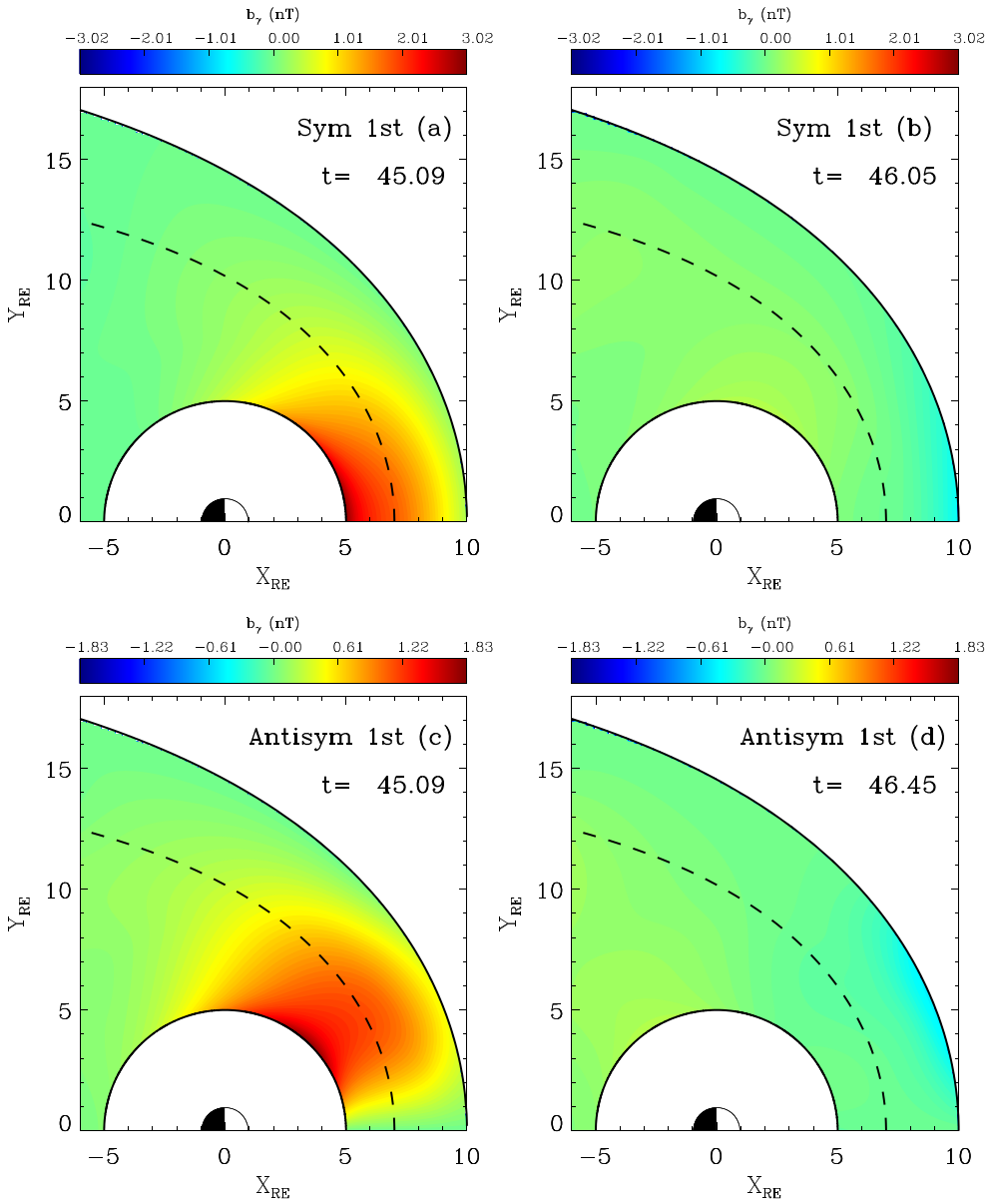

Figure 6. The variation of the compressional magnetic field perturbation in the equatorial plane on the dusk flank. Panels (a) and (b) show the first (radial) harmonic that is symmetric about noon. Panels (c) and (d) show the first (radial) harmonic that is antisymmetric about noon.

To study the structure of the symmetric (about noon) modes we apply the following steady oscillatory driver $b_\gamma(\beta,\gamma,t) = T(t)\cos^2(k_\beta\beta)\cos^2(k_\gamma\gamma)$, where noon is at $\beta = 0$ and

$$T(t) = \begin{cases} \sin^2(\pi t/\tau_d), & 0 \le t < \tau_d/2 \\ \sin(\pi t/\tau_d), & \tau_d/2 \le t < \tau_d/2 + 2\tau_d n_c \\ \sin^2(\pi t/\tau_d), & \tau_d/2 + 2\tau_d n_c \le t < \tau_d + 2\tau_d n_c \\ 0, & t \ge \tau_d + 2\tau_d n_c \end{cases} \tag{34}$$

where n_c is the number of periods which the simulation is driven for, $k_\beta = \pi/2$ and $k_\gamma = \pi/12$. (Note the different time dependence to the impulsive driver in equation (33).)

The period of the driver ($2\tau_d$) is based upon the frequency in the FFT in Figure 4. Figure 5a shows the variation of the compressional magnetic field perturbation at noon ((X,Y)=(6.79,0)) when driven at the frequency of the first symmetric harmonic. Since the mode is driven at its natural frequency, it responds by

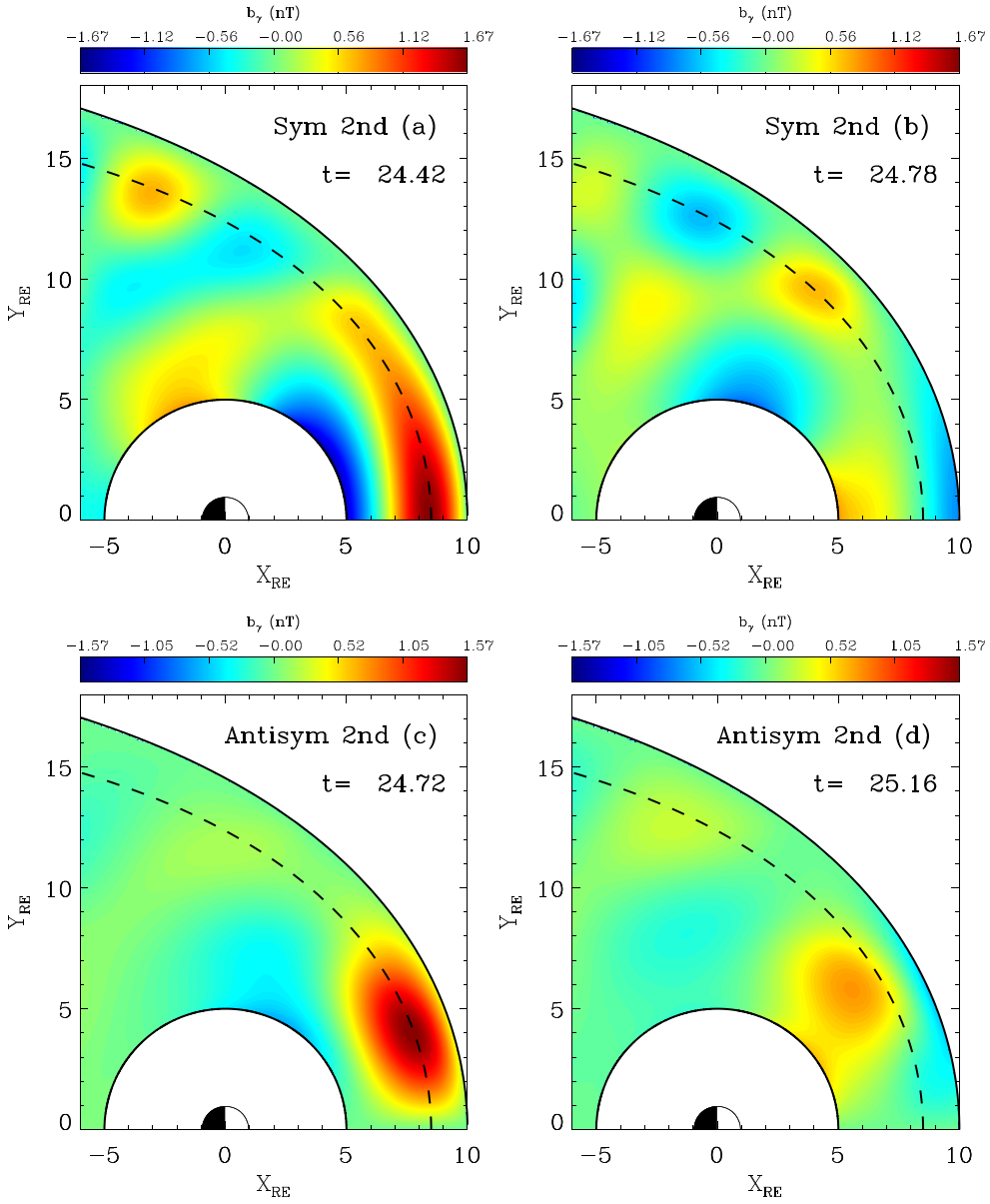

Figure 7. The same as Figure 6, but for the second radial harmonic.

growing secularly in time initially. The growth saturates and a balance is reached between the rate at which energy is supplied by the driver and the rate at which energy is lost through wave propagation into the tail and coupling to FLRs. The driver in Figure 5a was turned off at $t = 69.75$ min, and the rapid decay of the mode over a few cycles is evident. Since the fundamental symmetric mode is the only mode present, an FFT of the decay phase can be used to improve our estimate of the natural frequency. Indeed, Figure 5a is the result of rerunning the simulation with the improved frequency estimate. Figure 5c shows the equivalent results for the second symmetric harmonic.

For an antisymmetric driver (about noon) we employ

$$b_\gamma(\beta,\gamma,t) = \begin{cases} T(t)\sin\left(k_\beta\beta\right)\cos^2(k_\gamma\gamma), & 0 \le |\beta| < 0.5 \\ T(t)\sin^2(k_\beta\beta)\cos^2(k_\gamma\gamma), & 0.5 \le |\beta| < 1.0 \\ 0, & |\beta| > 1.0 \end{cases} \tag{35}$$

with the same time dependence as the symmetric case given by equation (34) used. Following a similar procedure to the symmetric modes, the antisymmetric modes can be studied. The results are shown

in Figures 5b and 5d. Note that these modes will have a node of b_γ at noon, so we show $b_\gamma(t)$ at (b) (X, Y)=(5.06, 4.53) and (d) (X, Y)=(7.77, 3.64)).

During the saturated phases evident in Figure 5 it is possible to study the structure of the waveguide modes in the equatorial plane by taking a couple of appropriate snapshots of b_γ. Elsden and Wright (2018) explain how two snapshots taken a quarter of a cycle apart can be thought of representing the real and imaginary parts of a complex variable $f(\alpha, \beta, \gamma) = b_\gamma(\alpha, \beta, \gamma, t_1) - ib_\gamma(\alpha, \beta, \gamma, t_1 + T_m/4)$, where T_m is the period of the mth mode, and t_1 is the time of the first snapshot. The structure of the mth mode may be described by

$$b_{\gamma m}(\alpha, \beta, \gamma, t) = f(\alpha, \beta, \gamma)e^{i\omega_r t}e^{-\omega_i t} \tag{36}$$

where $\omega = \omega_r + i\omega_i$ is the complex frequency of the mode (based on the period and decay rate of the undriven phases in Figure 5). The physical magnetic field that would be observed at any time may be taken as the real part of $b_{\gamma m}(\alpha, \beta, \gamma, t)$. Thus, two simulation snapshots a quarter of a cycle apart can be used to construct the full time dependent decay of a waveguide mode. Figure 6 shows two such snapshots of b_γ in the equatorial plane for the symmetric and antisymmetric first radial harmonic.

By using plots like Figure 4 to estimate the frequencies of the second radial harmonics, a similar procedure used to generate Figure 6 can be followed to show the spatial variation of b_γ in the equatorial plane. Figure 7 shows two snapshots for the second radial harmonics and allows the full time dependence, given by the real part of $b_{\gamma m}$, to be constructed using equation (36). The upper panels in Figure 7 show the second radial harmonic that is symmetric about noon, and the lower panels show the corresponding antisymmetric mode.

The values of the frequencies found in the FFTs for the symmetric driver which produced Figure 4 correspond, of course, to the first and second radial harmonic symmetric waveguide modes. The frequencies of 3.9 and 11.8 mHz can be appreciated as follows. Consider a uniform medium in which the fast mode frequency is given by $\omega = V_A(k_x^2 + k_y^2 + k_z^2)^{1/2}$. If the smallest dimension is the extent in x, suggesting $k_x \gg k_y, k_z$, then $\omega \approx V_A k_x$ (or $f \approx V_A/\lambda_x$). Thus, we can estimate the fast frequency based upon the wavelength and V_A for a uniform medium, as the ratio of these corresponds to the period—or travel time. As we have a nonuniform medium we need to estimate the travel time based upon $\int \mathrm{d}X/V_A(X, 0, 0)$. This gives a travel time between the subsolar point and the plasmapause (5,0,0) of 59.17 s (0.986 min). Note that in Figure 6a the variation of b_γ along the X axis goes from being a maximum ($X = 5$) to a node ($X = 10$), which corresponds to a quarter cycle. Hence, the radial fundamental period is expected to be around 4×0.986 min (equivalent to 4.2 mHz), in good agreement with the observed value of 3.9 mHz (given the resolution of the FFT and approximations in estimating the frequency). The frequency of the second harmonic is not double that of the first, but almost triple it. This can be understood by studying the variation of b_γ for the second radial harmonic between $X = 5$ and $X = 10$ along the X axis in Figure 7: It goes from minimum, to node, to maximum, to node, that is, 3/4 of a cycle compared to the 1/4 cycle of the first harmonic. Hence, the observed frequencies of 3.9 and 11.8 mHz differ by a factor of 3. This nodal structure is consistent with our boundary conditions of a node of u_α (antinode of b_γ) at the plasmapause and a node of b_γ at the magnetopause.

In section 4.3 we show how Figures 6 and 7, along with equation 36, can be used to examine the standing or propagating nature of the waveguide modes.

4.2. Field Line Resonances

The four waveguide modes in Figures 6 and 7 can couple to FLRs. Our ionospheric boundary conditions mean FLRs will always have an antinode of $j_\parallel$ at the ionosphere independent of whether they are an odd or even harmonic. To identify the location of Alfvén waves in the equatorial plane we plot $j_\parallel$ at the ionosphere mapped along the field line to the equatorial plane in Figure 8. Note how the waveguide modes that are symmetric about noon (i.e., they have a node of azimuthal magnetic pressure gradient at noon) have a node in the FLR amplitude at noon also (Figures 8a and 8c). In contrast the antisymmetric waveguide modes have an antinode of the azimuthal magnetic pressure gradient at noon, and hence drive FLRs very strongly at noon (Figures 8b and 8d).

The FLRs in our equilibrium will have a toroidal polarization, and their harmonic number can be identified by looking at the variation of $b_\beta(\alpha, \gamma)$ in a meridian plane. The dashed lines in Figure 8 show suitable planes, and Figure 9 shows the variation of b_β in these planes. In Figure 8a we see the first radial harmonic symmetric waveguide mode couples to an FLR centered on $L = 7.5$, and Figure 9a indicates this is a fundamental FLR. Similarly, the second radial harmonic symmetric waveguide mode couples to an FLR at $L = 8$

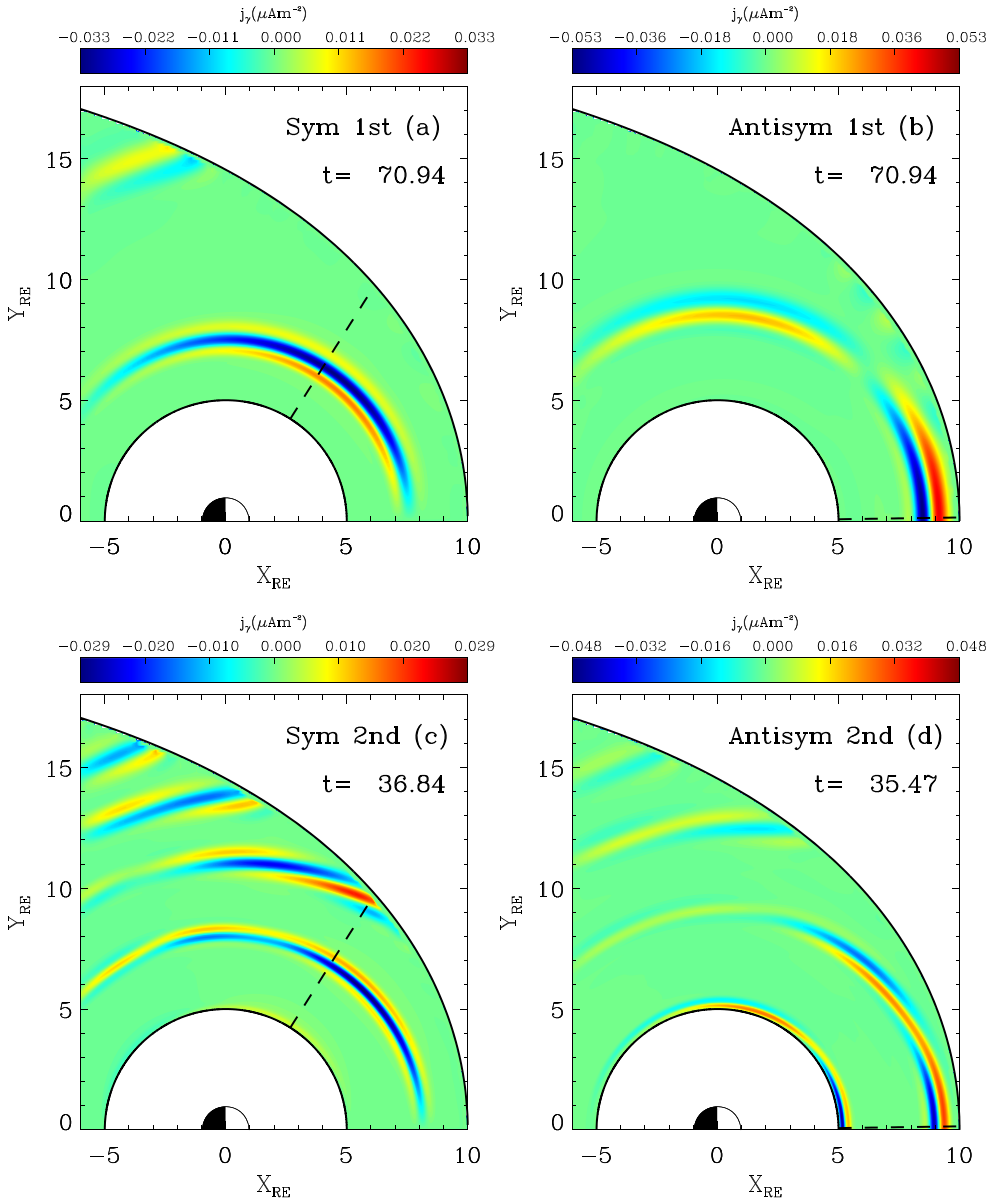

Figure 8. Location of Alfvén waves in the equatorial plane. The field-aligned current ($j_{||}$) at the ionospheric mapped along field lines to the equatorial plane. Panels (a) and (c) are for the first and second radial harmonics that are symmetric about noon (and so have a node of $j_{||}$ at noon). Panels (b) and (d) are for the first and second radial harmonics that are antisymmetric about noon (and so have an antinode node of $j_{||}$ at noon). The black dashed lines indicate meridian planes used in Figure 9.

(Figure 8c), and Figure 9c indicates this is a third harmonic FLR. (Note that there is a fifth harmonic FLR also excited by this waveguide mode at $L = 11$.)

The antisymmetric waveguide modes also couple to FLRs: The 1st radial harmonic mode drives an FLR at $L = 9$ (Figure 8b), and Figure 9b shows this to be the fundamental mode FLR. Similarly the second radial harmonic antisymmetric waveguide mode drives FLRs at $L = 5.5$ and $L = 9$ (Figure 8d), which Figure 9d shows to be the fundamental mode and third harmonic, respectively. We note Figure 8 also shows evidence of coupling to seventh and ninth harmonic FLRs on longer field lines. The results in Figure 9 are sensitive to the value of resistivity we use. In particular, the width in L shell scales as $\eta^{1/3}$, and we chose the value of η to give a realistic FLR width of about 1 R_E in the equatorial plane. The field-aligned structure of the FLRs was not found to vary noticeably with the value or spatial variation of η.

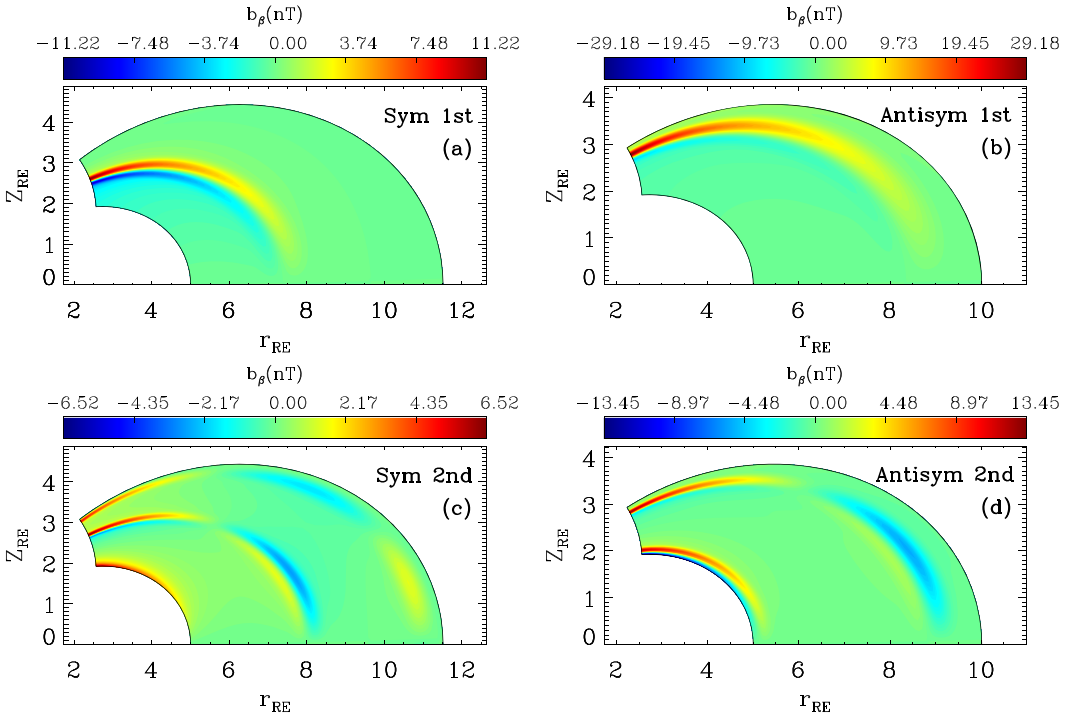

Figure 9. The variation of b_β (a signature of the Alfvén mode) in the meridional planes indicated by the dashed lines in Figure 8. These correspond to the FLRs excited by the following waveguide modes: (a) First radial harmonic that is symmetric about noon; (b) first radial harmonic that is antisymmetric about noon; (c) second radial harmonic that is symmetric about noon; (d) second radial harmonic that is antisymmetric about noon.

4.3. Azimuthally Standing/Propagating Waveguide Mode Nature

In a 2-D dipole model Elsden and Wright (2018) showed how the waveguide modes could have an azimuthally standing nature near noon and a tailward propagating nature on the flanks. In this subsection we study the phase relation between various simulation fields to see if this is true in the flaring flank magnetosphere we adopt here.

An initial insight can be gained by considering Figures 7a and 7b. In particular, the blue minima at (1, 11) in panel (a) has moved a quarter of a cycle later to (−1,13) in panel (b), and another quarter of a cycle later will be where the yellow maxima is at (−3,14) in panel (a). Evidently, the mode has a propagating character on the flank. The antinode evident at noon does not propagate in azimuth, but is standing in nature.

The wave-like nature of the modes comes from the following dominant terms in equation (31)

$$\frac{\partial B_\gamma}{\partial t} = -\frac{h_\gamma}{h_\alpha h_\beta}\left[\frac{\partial U_\alpha}{\partial \alpha} + \frac{\partial U_\beta}{\partial \beta}\right]. \tag{37}$$

In a uniform field the right-hand side of equation (37) reduces to $-\nabla \cdot u$. Moreover, in a Cartesian waveguide (with azimuthal coordinate y) a 1-D standing wave would have the spatial variations of B_γ and $-\nabla \cdot u$ (with y) being in phase. In contrast, these would be in quadrature for a propagating wave. To see if this is a useful diagnostic for interpreting the fast waveguide modes we show, in Figure 10, snapshots of B_γ and the right-hand side of (37) along the dashed lines indicated in Figures 6 and 7.

In Figure 10, "Distance" corresponds to path length along the dashed lines measured from noon. The red and black lines are in phase near noon indicating that all the modes have a standing nature here. Moving away from noon the phase relation is ambiguous, as is to be expected in a nonuniform medium. However, as we get to the more distant flank, the phase relation is closer to quadrature—indicative of a propagating wave. This is particularly clear in panel (c), which corresponds to the second radial harmonic that is symmetric about noon (Figures 7a and 7b) and was discussed at the start of this subsection. These results confirm the mode structure reported by Elsden and Wright (2019) for a 2-D dipole (namely, that waveguide modes

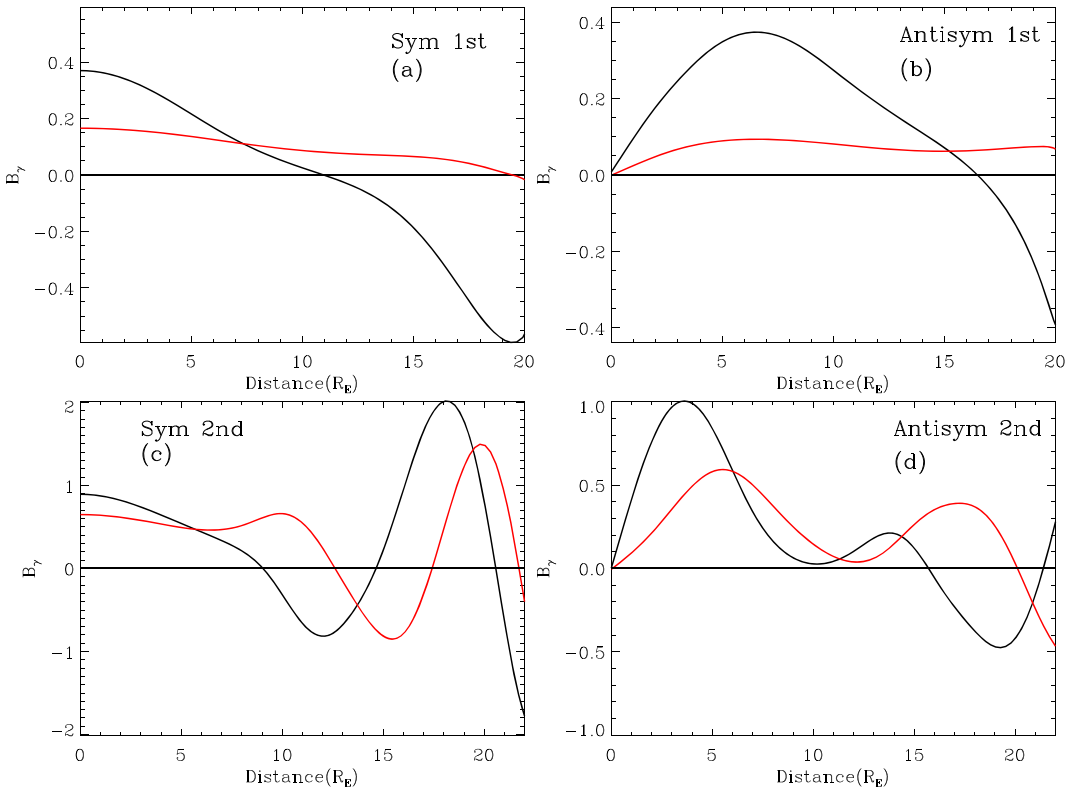

Figure 10. The variation of B_γ (black) and the right-hand side of equation (37) (red) along the dashed lines in Figure 6 for the first radial harmonic waveguide modes: (a) symmetric, and (b) antisymmetric about noon. Similar plots for the second radial harmonics of Figure 7 are shown in (c) symmetric, and (d) antisymmetric. The distance on the horizontal axis corresponds to path length along the dashed lines in Figures 6 and 7 measured from noon.

have a standing nature near noon, but propagating nature on the flanks) carries over to a 3-D dipole with flared flanks.

4.4. 3-D FLRs in a Plume

To illustrate the efficacy of our simulation for studying wave coupling in 3-D we use the highly asymmetric V_A associated with an afternoon plume as shown in Figure 11a (Borovsky & Denton, 2008). Such a situation has already been studied using a normal mode approach by Degeling et al. (2018), whose results showed the ability of FLRs to cross L shells. Here we adopt a time-dependent approach to complement that of Degeling et al. (2018). We drive the magnetopause with an impulsive symmetric magnetic pressure similar to that in equation (33).

The density is set through the Alfvén speed profile shown in Figure 11a (given the background dipole magnetic field). At the heart of the plume the Alfvén speed is approximately a factor of 3 lower than outside (but on the same L shell) and hence the density increases by a factor of 9. This is on the lower end of the density increase used in the plume in Figure 1 of Degeling et al. (2018).

Figure 11b shows $j_\parallel$ at the ionosphere plotted at the corresponding location in the equatorial plane. We use $j_\parallel$ as a proxy for the Alfvén wave as the fast mode does not carry strong field-aligned currents. There are some similarities with the Alfvén waves in Figures 8a and 8c which were also driven with a driver that was symmetric about noon: in both Figures 8a, 8c, and 11b the symmetric driver excites Alfvén waves with a node in the vicinity of noon.

The distribution and polarization of Alfvén waves is very different prenoon and postnoon. As shown in Elsden and Wright (2017), the frequency of the Alfvén waves along a given ridge in Figure 11b are the same. Thus, Alfvén waves near noon on the outer dashed circle ($r = 8\,R_e$) at $(X, Y) \approx (8, 2)$ lie on the blue ridge that moves to the inner dashed circle ($r = 6\,R_e$) at later MLT. Moreover, Wright and Elsden (2016) show that the Alfvén wave plasma displacement lies along (i.e., is tangential to) these ridges.

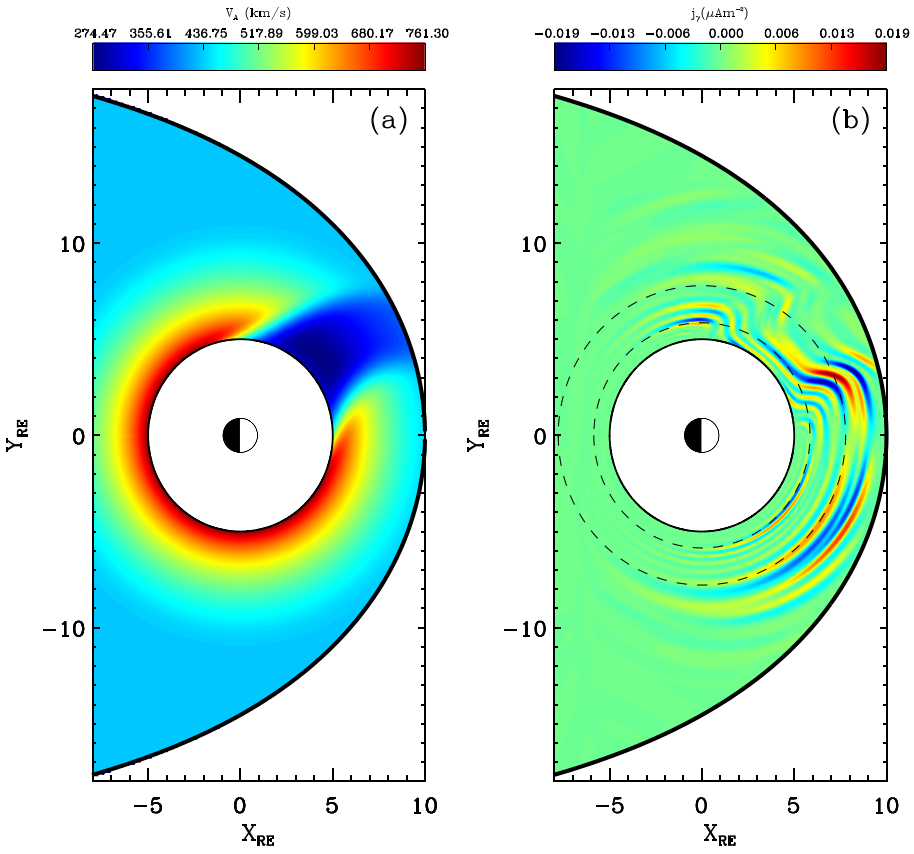

Figure 11. (a)The variation of V_A in the equatorial plane with a plume in the afternoon. There is an additional $\rho \propto r^{-4}$ variation along field lines. (b) $j_{||}$ at the ionosphere mapped along field lines to the equatorial plane. The dashed black lines are for reference and are at $r = 6$ and 8 R_e

It is not surprising that a toroidal Alfvén wave at $(X, Y) \approx (8, 2)$ and $(X, Y) \approx (4, 4)$, corresponding to $L = 8$ and $L = 6$, respectively, can have the same frequency: this is because the $L = 6$ field line is in a dense plume, so its Alfvén frequencies are lowered. What is surprising is that for a well phase-mixed Alfvén wave, the plasma displacement will be along the ridges in Figure 11 (see Figure 4 of Wright & Elsden, 2016). This means that the Alfvén waves at $(X, Y) \approx (8, 2)$ and $(X, Y) \approx (4, 4)$ will both have toroidal polarization. However, along the ridge joining these locations, the plasma displacement (i.e., polarization) is far from toroidal. In fact the FLR crosses from $L = 8$ to $L = 6$, and when at $L = 7$ has a plasma displacement that is at roughly 45° to the toroidal direction—that is, its polarization is neither poloidal or toroidal, but midway between.

The frequencies of toroidal and poloidal fundamental Alfvén modes differ by around 30% in a 3-D dipole field, and Wright and Elsden (2016) have shown how to calculate the frequency of an Alfvén wave of any intermediate polarization (see their equation (23) and Figure 6). It is evident that the FLRs in Figure 11 cannot be interpreted with the usual 2-D toroidal FLR theory. The 3-D nature of the equilibrium requires a theoretical description that is somewhat different to 2-D (Degeling et al., 2018; Wright & Elsden, 2016). Recall that Elsden and Wright (2017) showed that the frequency of Alfvén waves on a given ridge is the same everywhere along the ridge. Hence, when the FLR is crossing L shells it is adjusting its polarization angle such that its frequency (which depends upon this angle, Wright & Elsden, 2016) exactly matches the frequency found everywhere along that ridge.

Our results differ from those of Degeling et al. (2018) in that their solution was a normal mode, which excited a narrow FLR at the frequency of the mode. In contrast our time-dependent simulation has an impulsive broadband driver, which excites Alfvén waves over a wide range of field lines such that the range of the Alfvén continuum excited corresponds to the upper and lower bounds of the spectrum of the impulsive driver (Mann et al., 1995).

5. Concluding Remarks

We have described a novel simulation model for studying the coupling of MHD waves in a nonuniform 3-D magnetosphere with flared flanks. The model is well suited to studying the propagation of waves from the dayside around the flanks and to the near-Earth nightside. A major consideration in our model is optimizing the grid for computational efficiency. We also devise a suitable magnetopause boundary condition such that this boundary need not coincide with a coordinate surface.

The waveguide modes of the system are central to understanding the response of the magnetosphere to a variety of driving conditions, and we calculate the lowest order modes for a simple V_A model. The modes have a standing nature near noon, but switch to a propagating character on the flanks and into the tail. The frequencies of the waveguide modes is of great importance as this identifies the frequencies that FLRs are preferentially excited with (Wright, 1994).

Finally, we show results from an impulsively driven highly asymmetric equilibrium containing a plume in the afternoon. Our results can be interpreted using 3-D Alfvén resonance theory, and show how FLRs can cross L shells with a polarization that is neither toroidal or poloidal. In our model the FLRs cross 2 L shells at an angle of around 45° over a local time of 1–2 hr. This sort of behavior cannot be understood with 2-D FLR theory.

Acknowledgments
A. N. W. was partially funded by STFC (ST/N000609/1) and the Leverhulme Trust (RPG-2016-071). T. E. was funded by the Leverhulme Trust (RPG-2016-071) and a Leverhulme Trust Early Career Fellowship (ECF-2019-155). The research in this paper was completed as part of the activities of an International Team sponsored by the International Space Science Institute (ISSI, Bern). The authors are grateful to ISSI for supporting this work. Data used to produce the simulation plots can be accessed at this site (https://figshare.com/authors/Tom_Elsden/4743264).

References

Angerami, J. J., & Carpenter, D. L. (1966). Whistler studies of the plasmapause in the magnetosphere: 2. Electron density and total tube electron content near the knee in magnetospheric ionization. *Journal of Geophysical Research*, *71*, 711–725.

Archer, M. O., Hartinger, M. D., Walsh, B. M., Plaschke, F., & Angelopoulos, V. (2015). Frequency variability of standing Alfvén waves excited by fast mode resonances in the outer magnetosphere. *Geophysical Research Letters*, *42*, 10,150–10,159. https://doi.org/10.1002/2015GL066683

Borovsky, J. E., & Denton, M. H. (2008). A statistical look at plasmaspheric drainage plumes. *Journal of Geophysical Research*, *113*, A09221. https://doi.org/10.1029/2007JA012994

Claudepierre, S. G., Hudson, M. K., Lotko, W., Lyon, J. G., & Denton, R. E. (2010). Solar wind driving of magnetospheric ULF waves: Field line resonances driven by dynamic pressure fluctuations. *Journal of Geophysical Research*, *115*, A11202. https://doi.org/10.1029/2010JA015399

Degeling, A. W., Rae, I. J., Watt, C. E. J., Shi, Q. Q., Rankin, R., & Zong, Q.-G. (2018). Control of ULF wave accessibility to the inner magnetosphere by the convection of plasma density. *Journal of Geophysical Research: Space Physics*, *123*, 1086–1099. https://doi.org/10.1002/2017JA024874

Degeling, A. W., Rankin, R., Kabin, K., Rae, I. J., & Fenrich, F. R. (2010). Modeling ULF waves in a compressed dipole magnetic field. *Journal of Geophysical Research*, *115*, A10212. https://doi.org/10.1029/2010JA015410

Ellington, S. M., Moldwin, M. B., & Liemohn, M. W. (2016). Local time asymmetries and toroidal field line resonances: Global magnetospheric modeling in SWMF. *Journal of Geophysical Research: Space Physics*, *121*, 2033–2045. https://doi.org/10.1002/2015JA021920

Elsden, T., & Wright, A. N. (2017). The theoretical foundation of 3-D Alfvén resonances: Time-dependent solutions. *Journal of Geophysical Research: Space Physics*, *122*, 3247–3261. https://doi.org/10.1002/2016JA023811

Elsden, T., & Wright, A. N. (2018). The broadband excitation of 3-D Alfvén resonances in a MHD waveguide. *Journal of Geophysical Research: Space Physics*, *123*, 530–547. https://doi.org/10.1002/2017JA025018

Elsden, T., & Wright, A. N. (2019). The effect of fast normal mode structure and magnetopause forcing on FLRs in a 3-D waveguide. *Journal of Geophysical Research: Space Physics*, *124*, 178–196. https://doi.org/10.1029/2018JA026222

Kageyama, A., Sugiyama, T., Watanabe, K., & Sato, T. (2006). A note on the dipole coordinates. *Computers and Geosciences*, *32*, 265–269.

Kivelson, M. G., & Southwood, D. J. (1988). Hydromagnetic waves and the ionosphere. *Geophysical Research Letters*, *15*, 1271–1274.

Lee, D.-H., & Lysak, R. L. (1989). Magnetospheric ULF wave coupling in the dipole model—The impulsive excitation. *Journal of Geophysical Research*, *94*, 17,097–17,103.

Lysak, R. L., Song, Y., Sciffer, M. D., & Waters, C. L. (2015). Propagation of Pi2 pulsations in a dipole model of the magnetosphere. *Journal of Geophysical Research: Space Physics*, *120*, 355–367. https://doi.org/10.1002/2014JA020625

Mann, I. R., Wright, A. N., & Cally, P. S. (1995). Coupling of magnetospheric cavity modes to field line resonances: A study of resonance widths. *Journal of Geophysical Research*, *100*, 19,441–19,456.

Moore, T. E., Gallagher, D. L., Horwitz, J. L., & Comfort, R. H. (1987). MHD wave breaking in the outer plasmasphere. *Geophysical Research Letters*, *14*, 1007–1010.

Proehl, J. A., Lotko, W., Kouznetsov, I., & Geimer, S. D. (2002). Ultralow-frequency magnetohydrodynamics in boundary-constrained geomagnetic flux coordinates. *Journal of Geophysical Research*, *107*(A9), 1225. https://doi.org/10.1029/2001JA000135

Shue, J.-H., Chao, J. K., Fu, H. C., Russell, C. T., Song, P., Khurana, K. K., & Singer, H. J. (1997). A new functional form to study the solar wind control of the magnetopause size and shape. *Journal of Geophysical Research*, *102*, 9497–9512.

Swisdak, M. (2006). Notes on the dipole coordinate system. arXiv Physics e-prints.

Takahashi, K., & Anderson, B. J. (1992). Distribution of ULF energy ($f < 80$ mHz) in the inner magnetosphere: A statistical analysis of AMPTE CCE magnetic field data. *Journal of Geophysical Research*, *97*, 10.

Woodroffe, J. R., & Lysak, R. L. (2012). Ultra-low frequency wave coupling in the ionospheric Alfvén resonator: Characteristics and implications for the interpretation of ground magnetic fields. *Journal of Geophysical Research*, *117*, A03223. https://doi.org/10.1029/2011JA017057

Wright, A. N. (1994). Dispersion and wave coupling in inhomogeneous MHD waveguides. *Journal of Geophysical Research*, *99*, 159–167.

Wright, A. N., & Elsden, T. (2016). The theoretical foundation of 3D Alfvén resonances: Normal modes. *Astrophysical Journal*, *833*, 230.
Wright, A. N., & Rickard, G. J. (1995). A numerical study of resonant absorption in a magnetohydrodynamic cavity driven by a broadband spectrum. *Astrophysical Journal*, *444*, 458.
Zalesak, S. T. (1979). Fully multidimensional flux-corrected transport algorithms for fluids. *Journal of Computational Physics*, *31*, 335–362.